

# Invisible Needle Detection in Ultrasound: Leveraging Mechanism-Induced Vibration

Chenyang Li<sup>\*1</sup>, Dianye Huang<sup>\*1</sup>, Angelos Karlas<sup>2,3,4</sup>, Nassir Navab<sup>1</sup>, and  
Zhongliang Jiang<sup>\*\*1</sup>

<sup>1</sup> Chair for Computer Aided Medical Procedures and Augmented Reality, Technical  
University of Munich, Munich, Germany

<sup>2</sup> Institute of Biological and Medical Imaging, Helmholtz Zentrum Munchen,  
Neuherberg, Germany

<sup>3</sup> School of Medicine, Central Institute for Translational Cancer Research  
(TranslaTUM), Technical University of Munich, Munich, Germany

<sup>4</sup> Department for Vascular and Endovascular Surgery, Klinikum rechts der Isar,  
Technical University of Munich, Munich, Germany

**Abstract.** In clinical applications that involve ultrasound-guided intervention, the visibility of the needle can be severely impeded due to steep insertion and strong distractors such as speckle noise and anatomical occlusion. To address this challenge, we propose VibNet, a learning-based framework tailored to enhance the robustness and accuracy of needle detection in ultrasound images, even when the target becomes invisible to the naked eye. Inspired by Eulerian Video Magnification techniques, we utilize an external step motor to induce low-amplitude periodic motion on the needle. These subtle vibrations offer the potential to generate robust frequency features for detecting the motion patterns around the needle. To robustly and precisely detect the needle leveraging these vibrations, VibNet integrates learning-based Short-Time-Fourier-Transform and Hough-Transform modules to achieve successive sub-goals, including motion feature extraction in the spatiotemporal space, frequency feature aggregation, and needle detection in the Hough space. Based on the results obtained on distinct *ex vivo* porcine and bovine tissue samples, the proposed algorithm exhibits superior detection performance with efficient computation and generalization capability.

**Keywords:** Ultrasound images · needle detection · temporal analysis.

## 1 Introduction

Ultrasound-guided percutaneous needle insertion is widely used in clinical practices [7], such as drug delivery, regional anesthesia, and tissue biopsy. Compared with CT and MRI, ultrasound (US) is real-time and radiation-free. However, inherited limitations such as speckles, noise, and low resolution make it challenging

---

\* Contribute equally

\*\* Corresponding author

to robustly track the percutaneous needle. Furthermore, for 2D US images, a certain level of skill is required to maintain the aligned pose during the insertion process. Misalignment can occur, causing the needle to become invisible. Additionally, a steep insertion angle can also impede needle visibility due to the US wave propagation theory [12]. These factors can severely impair the performance on segmenting and tracking needles that are inserted beneath the skin.

To enhance the needle visibility, Cheung *et al.* steered the US beam to be perpendicular to the inserted needle [3]. The results show the method can significantly improve the needle visibility by maximizing the received reflections. However, the majority of commercial US systems do not provide access to low-level parameters, such as steering angles. Alternatively, Harmat *et al.* first employed power Doppler images to facilitate the detection of needles in US images [4]. Jiang *et al.* designed an ultrasonic needle-actuating device using piezoelectric material [6]. To have reliable Doppler effects assisting the needle segmentation, the vibration should be performed at a high frequency, which is usually over  $15K\ Hz$ . Besides, Beigi *et al.* further investigated the possibility of using natural tremors during needle insertion based on temporal analysis of pixel phase variations [1]. This novel approach is promising to be integrated into current clinical practices, while the pre- and post-processing procedures required to reveal subtle tremors of operators are computationally expensive.

To reveal subtle motion, Wu *et al.* first introduced the idea of Euler Video Magnification (EVM) through spatio-temporal processing to magnify the subtle movements in the natural image sequence [16]. To further address the challenge posed by non-stationary objects, Zhang *et al.* proposed a method to only magnify the acceleration term [17]. An initial trial of applying EVM on ultrafast US images has been shown in [11]. In conventional US systems, Huang *et al.* employed a robotic system to stabilize the movement of the probe during artery scanning, enabling the extraction of subtle pulsation signals according to heartbeats [5].

This study presents a deep-learning framework, VibNet, that can enhance the robustness and accuracy of detecting thin needles in US images by leveraging vibratory motions applied externally on the needle shaft. Unlike conventional methods that rely on image intensity, VibNet uses frequency features, thereby maintaining effectiveness even when thin objects become imperceptible in US images. To the best of our knowledge, this is the first deep learning-based approach detecting needles on US images leveraging the information from external vibration. In this study, the proposed VibNet consists of three modules: temporal feature extraction, frequency feature aggregation, and needle detection. To validate the performance of the proposed method, experiments were performed on different *ex vivo* samples. The results demonstrate that both robustness and detection accuracy are enhanced, even when the needle becomes invisible in extreme cases.

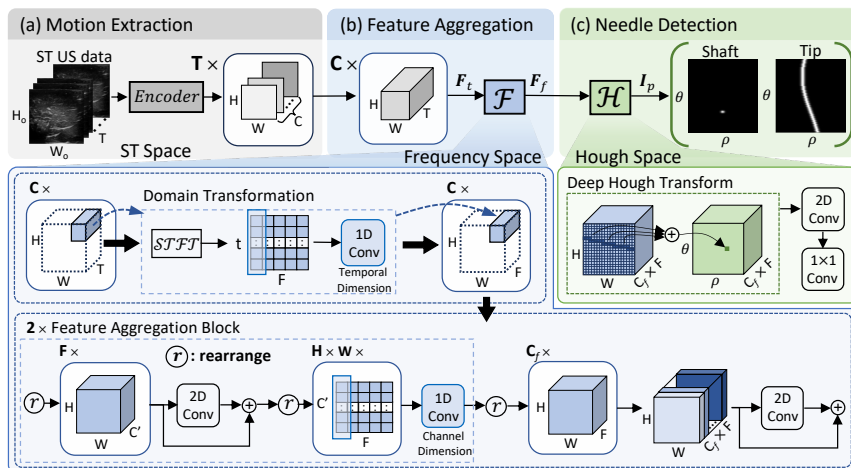


**Fig. 1.** Overview of VibNet, comprising modules for (a). Motion feature extraction, (b). Frequency feature aggregation, and (c). Needle shaft and tip localization.

## 2 Method

The overall structure of VibNet is demonstrated in Fig. 1. A series of consecutive US images are used as input, and the output two-channel images indicating the needle shaft and tip are obtained by a set of processes in three feature spaces.

### 2.1 Vibration Encoding from Sequential US Images

To characterize the subtle vibration of the needle, sequential US images  $\mathbf{I} \in \mathbb{R}^{H_o \times W_o \times T}$  are used as inputs. Instead of using hand-designed decomposition filters, such as complex steerable filters [14], a CNN-based encoder is applied here to extract the representation in order to circumvent the complexity of hand-craft filters and to enhance the time efficiency. To enhance the sensitivity for motions in consecutive images, a pre-trained encoder  $E_{shape}(\mathbf{I})$  presented by Oh *et al.* [10] based on extensive synthetic data with moving objects is used. Repeating this feature extraction process for  $T$  images, a feature representation  $\mathbf{S} \in \mathbb{R}^{T \times C_o \times H \times W}$  for sequential data can be computed. Then, we apply a 1D convolution,  $\mathbf{F}_t = Conv_{1d}(\mathbf{S})$ , in the dimension of the feature channel to compress the number of features ( $C_o \rightarrow C$ ) while maintaining spatial-temporal correspondence to original inputs.

### 2.2 Frequency Feature Aggregation

**Domain Transformation.** Specific to thin objects like needles, their visibility is severely affected by the US speckle noise, tissue artifacts, etc. Unlike the image intensity, the periodic vibration pattern in the frequency domain is more robust

and distinctive, even when the needle is slightly out of the US plane. To extract the feature in the frequency domain, a 1-D convolution layer with  $k$  kernels is employed to decompose the series data into varying frequency ranges. To provide time-localized frequency information, the idea of Short-Time-Fourier-Transform (STFT) is applied on  $\mathbf{F}_t$  in the temporal dimension ( $C \times * \times H \times W$ ). Inspired by the Fourier-initialized convolution (FIC) layer [8], the 1D convolution kernels  $\mathbf{W}_{[k,n]}$  are initialized as below:

$$\mathbf{W}_{[k,n]} = \exp(-j2\pi kn/N) \quad (1)$$

where  $N$  is the number of elements in each kernel, mimicking the sliding window in STFT,  $n = 0, 1, 2, \dots, N - 1$  is the sample indices within the window.  $k = 0, 1, 2, \dots, N - 1$  generates varying decomposing frequencies. After applying the learnable  $\mathbf{W}_{[k,n]}$  to each individual temporal series input, a set of 2D spectrograms described in both temporal  $t$  and frequency  $F$  dimension are obtained. Then, another 1D convolution is used to compress the temporal series at each sampling frequency to obtain the frequency feature representation in the dimensional of ( $C \times F \times H \times W$ ).

**Frequency Feature Aggregation.** To extract features representing different motion patterns, we aggregate the multi-channel feature map by conducting convolutions alternately on the spatial and channel dimensions. The identical block is repeated twice for feature aggregation, which comprises a 2D ResBlock that perceives motion patterns of the neighboring pixels and a subsequent 1D convolution layer that mixes features from multiple channels. The proposed frequency feature aggregation module, denoted as  $\mathbf{F}_f = \mathcal{F}(\mathbf{F}_t)$ , concludes with a 2D ResBlock, yielding an aggregated feature  $\mathbf{F}_f \in \mathbb{R}^{(C_f \cdot F) \times H \times W}$ .

### 2.3 Needle Shaft and Tip Localization

The Hough Transform can robustly detect a discontinuous straight line. Hence, we employ a deep Hough Transform (HT) [18] module to map the features from the frequency space to the Hough space. Subsequently, a set of 2D convolutions is performed to aggregate the features spatially. A  $1 \times 1$  2D convolution layer is finally employed to produce a two-channel prediction image  $\mathbf{I}_p$  in the Hough space where the shaft is presented as a single point in the first channel  $\mathbf{I}_p^1$ ; the tip is presented as a sinusoidal wave in the second channel  $\mathbf{I}_p^2$ . The process of needle determination is denoted as  $\mathbf{I}_p = \mathcal{H}(\mathbf{F}_f)$ . In this study, HT is conducted in the frequency space rather than the typical ST space to take full advantage of more reliable frequency features rather than relying on susceptible intensity values. It is noteworthy that VibNet remains effective, as the consistency of the image size is maintained throughout feature aggregation.

**Post Processing.** To locate the needle shaft and tip in the image space, the prediction  $\mathbf{I}_p$  is further processed by using the following equation.

$$(\theta_s, \rho_s) = \arg \max_{\theta, \rho} \mathbf{I}_p^1; (x_t, y_t) = \arg \max_{x, y} \sum_{\theta_i, \rho_i \in \Theta_{\mathbf{I}_p^2}} i\mathcal{HT}\left(I_p^2(\theta_i, \rho_i), \theta_i, \rho_i\right) \quad (2)$$

where each pixel intensity in  $\mathbf{I}_p^1$  represents the probability of the current pixel being the target shaft location; while in  $\mathbf{I}_p^2$ , it represents the probability of its corresponding line in the image space intersecting with the target tip location;  $i\mathcal{HT}(\cdot)$  denotes the probability-weighted inverse HT operation,  $I_p^2(\theta_i, \rho_i)$  is the pixel intensity of  $\mathbf{I}_p^2$  indexed by  $\theta_i, \rho_i$ , and  $\Theta_{\mathbf{I}_p^2}$  is a collection of the pixel positions corresponding to top  $p\%$  pixel intensities in  $\mathbf{I}_p^2$ .

The pixel with the highest intensity in  $\mathbf{I}_p^1$  determines the shaft location  $(\theta_s, \rho_s)$ . For the tip detection, all elements in  $\Theta_{\mathbf{I}_p^2}$  are projected back into the original image space. These inverted images are then weighted by the corresponding pixel intensities in the Hough space and summed up to generate a new image. Finally, the pixel with the highest intensity in this image determines the tip location  $(x_t, y_t)$ . An intuitive illustration of the post-processing procedures is depicted in Fig. 2.

## 2.4 Resolving Class Imbalance

Since the needle shaft in the image space corresponds to a single point in the Hough space, the training suffers from severe class imbalance. To alleviate this issue, two approaches are used in this study.

**Gaussian-Shaped Ground Truth.** We render a Gaussian-shaped peak into the shaft ground truth images with a 2D Gaussian kernel and utilize a 1D Gaussian kernel to blur the tip ground truth image row-by-row. These Gaussian kernels assign Gaussian distributed probabilities to pixels adjacent to the ground truth, thereby taking inevitable labeling errors into account. Moreover, the learning of the model can be accelerated, as the neighborhood of the ground truth may have similar motion patterns.

**Focal Loss Function.** Compared with the standard Binary Cross-Entropy loss, we use Focal Loss [9] in this study. It can increase the relative weight for challenging samples whose predictions significantly differ from the ground truth. The final loss are structured as follows:  $L_{total} = \gamma L_{shaft} + (1 - \gamma)L_{tip}$ , where  $L_{shaft}$  and  $L_{tip}$  are the modified Focal Loss from [19], and  $\gamma = 0.7$  is a hyper-parameter that balances the shaft and tip prediction losses.

### 3 Experiments

#### 3.1 Implementation Details

**Experimental Setup** The US images were captured at 30 *fps* using the Siemens Juniper US Machine (ACUSON Juniper, SIEMENS AG, Germany). The inserted needle (18 *G*, length: 90 *mm*) was slightly vibrated at approximately 2.5 *Hz* by a step motor (RHOS, 28BYJ-48 - 5V; rotating back and forth at 5.625 *deg*) controlled by a micro control unit (STM32F103C8T6, STMicroelectronics NV, Switzerland), see Fig. 2. Inspired by Cheung *et al.* [3], the shaft and tip of the invisible needle were labeled by manually adjusting the US beam steering angle until the needle was optimally visualized. The training was performed on a desktop PC with one GPU (Nvidia GeForce RTX 4070) and one CPU (Intel® Core™ i7-13700KF Processor). The model was trained using an Adam optimizer with learning rate 1e-3, betas (0.9, 0.999).

**Dataset** A total of 417 ten-second US videos were recorded, comprising 206 and 211 videos from *ex vivo* porcine and bovine tissue samples, respectively. Each US video documents the beam steering adjustment process for labeling and records the vibration of the inserted needle (could be visually invisible) for training purposes. The dataset is divided into training (80%) and test (20%) sets. The training set contains 164 porcine videos (32699 sequences) and 168 bovine videos (35323 sequences), while the test set contains 42 porcine videos (8384 sequences) and 43 bovine videos (8944 sequences). Each sequence has 30 frames with dimensions of  $328 \times 335$  ( $H \times W$ ).

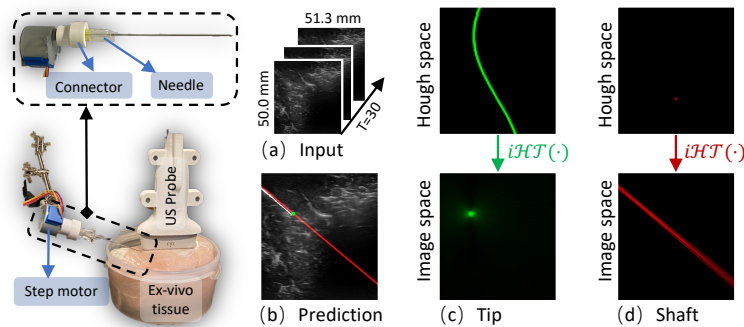


**Fig. 2.** An illustration of *Left*: the setup for data collection and *Right*: the intermediate results during inference. In (b), the green dot & red line and the white line indicate the predicted tip & shaft location and the ground truth, respectively.

### 3.2 Results and Discussion

**Evaluation Metrics.** In this section, we compared the performance of VibNet with UNet [13] and WNet [2] for the task of needle detection in terms of the error of needle tip position and insertion angle. All networks are trained on the bovine data. To highlight the superiority of our proposed method, we manually categorized the 43 test bovine videos into two groups: normal (27 videos) and challenging (16 videos). In the challenging videos, it is difficult for humans to discern the pixel intensity variations surrounding the vibrating needle. In addition, we denote predictions with large errors as outliers using the thresholds: angle error over  $90^\circ$  and tip error over  $150\text{ mm}$ .

Table 1 presents the performance of the three networks with the *mean*  $\pm$  *std* computed after excluding the outliers. VibNet performs the best, with the lowest percentage of outliers and prediction errors. This can be attributed to two factors: 1) utilizing longer input sequences and 2) processing input data in three distinct spaces. The superiority of longer input sequences is evidenced by comparing the performance on the challenging dataset. Additionally, evidence of the latter factor is analyzed in the ablation study.

**Table 1.** Performance comparison of the proposed VibNet with UNet&WNet-based needle detection frameworks. All networks are trained and tested on the bovine data.

Method	Test Dataset	Angle Error	Tip Error	Outlier	Inference
UNet [13]	Normal	2.53 $\pm$ 8.35	4.36 $\pm$ 5.34	0.73	<b>5.02<math>\pm</math>2.52</b>
	Challenging	4.58 $\pm$ 8.58	5.36 $\pm$ 4.49	15.05	
WNet [2]	Normal	2.00 $\pm$ 2.67	4.30 $\pm$ 4.65	0.00	16.71 $\pm$ 3.48
	Challenging	5.85 $\pm$ 11.17	5.70 $\pm$ 6.10	0.21	
VibNet (ours)	Normal	<b>1.21<math>\pm</math>1.15</b>	<b>1.20<math>\pm</math>1.12</b>	<b>0.00</b>	72.27 $\pm$ 3.98
	Challenging	<b>3.97<math>\pm</math>8.85</b>	<b>1.78<math>\pm</math>3.21</b>	<b>0.03</b>	

**Units:** Angle Error ( $^\circ$ ), Tip Error (mm), Outlier (%), Inference (ms)

**Evaluation on Generalizability.** We further assessed the generalizability of VibNet by training and testing the model on data recorded from two different *ex vivo* animal tissues (see Table 2). Notably, the model trained on one data maintains good detection performance on the other unseen animal data. This finding suggests that the proposed method has the potential to be extrapolated to unseen data. In addition, the results indicate that the model trained on bovine data performs better when applied to porcine data, even resulting in fewer outliers than the model directly trained on porcine data. This is because the bovine images are relatively dark, which makes the vibration become less visible. So, the extrapolation to a relatively easy case (porcine images with more visible vibration) can maintain good performance.

**Table 2.** Evaluations on the generalizability of the proposed VibNet.

Train \ Test	Porcine data			Bovine data		
	Angle Error	Tip Error	Outlier	Angle Error	Tip Error	Outlier
Porcine data	1.50±3.56	1.30±1.47	0.06	3.79±9.84	2.72±5.35	0.74
Bovine data	1.74±2.19	1.52±1.90	0.00	2.19±5.35	1.40±2.17	0.01

Units: Angle Error (°), Tip Error (mm), Outlier (%)

**Ablation Study.** An ablation study was conducted on VibNet to quantify the contribution of each module to the needle detection task. To demonstrate the necessity of transforming the input data into three distinct spaces, we retrained VibNet under three conditions: *i*). without initializing the encoder using the pre-trained parameters from [10], *ii*). without initializing the STFT modules using (1), *iii*). replacing the Deep HT module with a segmentation module. Moreover, to highlight the importance of integrating learning modules, a needle detection framework denoted as “VibNet\*–” was constructed, where all learnable modules of VibNet were replaced with Riesz pyramid [15], bandpass filters, and HT.

Table 3 shows the ablation results. It’s worth noting that without using any learnable modules, “VibNet\*–” performs the second worst. Significant performance degradation is observed when removing the Fourier initialization (w/o STFT init.), which implies that transforming the intensity variations into the frequency domain plays a crucial role in the proposed framework. Conversely, randomly initializing the encoder (w/o Enc. init.) results in good detection results, only with a small drop in terms of angular error. This small drop can be explained by the fact that compared to learning the weights from scratch, the encoder directly using the pretrained weights from [10] prevails in revealing motion areas and thus leads to better performance. In addition, it can be seen that the model replacing the Deep HT with a segmentation subnetwork (rp. Deep HT) also achieves good performance both in angular and tip error. However, the proposed VibNet can still outperform them in terms of both metrics, and with fewer outliers. These results demonstrate that HT is a better way to aggregate features by considering the geometric constraint that the needle presents as a straight line in images.

## 4 Conclusion

This paper introduces VibNet, a novel approach aimed at improving the precision and robustness of needle detection in US images. Unlike conventional methods that rely on image intensity, VibNet detects vibrations in frequency space, thereby maintaining effectiveness even when thin objects become imperceptible in US images. The results on two distinct *ex vivo* animal samples demonstrate VibNet’s capability of generalization. The ablation studies further demonstrate that the proposed method can result in the best performance in terms of both detection accuracy and outlier reduction. Further considering the time efficiency



**Table 3.** Results for Ablation study. Performance Comparison of different frameworks trained on the bovine data and tested on the porcine data.

Method	Angle Error (°)	Tip Error (mm)	Outlier (%)
VibNet w/o Enc. init.	2.72±5.04	1.53±2.09	<b>0.00</b>
VibNet w/o STFT init.	19.21±25.51	8.75±9.11	15.48
VibNet rp. Deep HT	1.95±2.27	1.78±2.13	0.06
VibNet* <sup>-</sup>	8.16±10.88	<i>N/A</i>	0.48
VibNet (ours)	<b>1.74±2.19</b>	<b>1.52±1.90</b>	<b>0.00</b>

w/o: without, rp.: replace, \*<sup>-</sup>: rp. all learnable modules, *N/A*: not applicable

for clinical translation, VibNet conducts an inference on an average of 72.3 *ms*. In future research, we will continue exploring methods for reliably detecting the single intersection point in the scenario of out-of-plane needle insertion.

## References

1. Beigi, P., Rohling, R., Salcudean, T., Lessoway, V.A., Ng, G.C.: Detection of an invisible needle in ultrasound using a probabilistic svm and time-domain features. *Ultrasonics* **78**, 18–22 (2017)
2. Chen, S., Lin, Y., Li, Z., Wang, F., Cao, Q.: Automatic and accurate needle detection in 2d ultrasound during robot-assisted needle insertion process. *International Journal of Computer Assisted Radiology and Surgery* pp. 1–9 (2022)
3. Cheung, S., Rohling, R.: Enhancement of needle visibility in ultrasound-guided percutaneous procedures. *Ultrasound in medicine & biology* **30**(5), 617–624 (2004)
4. Harmat, A., Rohling, R.N., Salcudean, S.E.: Needle tip localization using stylet vibration. *Ultrasound in medicine & biology* **32**(9), 1339–1348 (2006)
5. Huang, D., Bi, Y., Navab, N., Jiang, Z.: Motion magnification in robotic sonography: enabling pulsation-aware artery segmentation. In: 2023 IEEE/RSJ International Conference on Intelligent Robots and Systems (IROS). pp. 6565–6570. IEEE (2023)
6. Jiang, T., McLeod, G., Huang, Z., Zhu, X., Jiao, Y., Li, X., Shen, Z., Cui, Y.: Localization accuracy of ultrasound-actuated needle with color doppler imaging (vol 10, 1020, 2020). *DIAGNOSTICS* **11**(5) (2021)
7. Kuang, Y., Hilgers, A., Sadiq, M., Cochran, S., Corner, G., Huang, Z.: Modelling and characterisation of a ultrasound-actuated needle for improved visibility in ultrasound-guided regional anaesthesia and tissue biopsy. *Ultrasonics* **69**, 38–46 (2016)
8. Li, S., Chowdhury, R.R., Shang, J., Gupta, R.K., Hong, D.: Units: Short-time fourier inspired neural networks for sensory time series classification. In: Proceedings of the 19th ACM Conference on Embedded Networked Sensor Systems. pp. 234–247 (2021)
9. Lin, T.Y., Goyal, P., Girshick, R., He, K., Dollár, P.: Focal loss for dense object detection. In: Proceedings of the IEEE international conference on computer vision. pp. 2980–2988 (2017)
10. Oh, T.H., Jaroensri, R., Kim, C., Elgharib, M., Durand, F., Freeman, W.T., Matusik, W.: Learning-based video motion magnification. In: Proceedings of the European Conference on Computer Vision (ECCV). pp. 633–648 (2018)

11. Perrot, V., Salles, S., Vray, D., Liebgott, H.: Video magnification applied in ultrasound. *IEEE Transactions on Biomedical Engineering* **66**(1), 283–288 (2018)
12. Reusz, G., Sarkany, P., Gal, J., Csomos, A.: Needle-related ultrasound artifacts and their importance in anaesthetic practice. *British journal of anaesthesia* **112**(5), 794–802 (2014)
13. Ronneberger, O., Fischer, P., Brox, T.: U-net: Convolutional networks for biomedical image segmentation. In: *Medical Image Computing and Computer-Assisted Intervention–MICCAI 2015: 18th International Conference, Munich, Germany, October 5–9, 2015, Proceedings, Part III* 18. pp. 234–241. Springer (2015)
14. Wadhwa, N., Rubinstein, M., Durand, F., Freeman, W.T.: Phase-based video motion processing. *ACM Transactions on Graphics (ToG)* **32**(4), 1–10 (2013)
15. Wadhwa, N., Rubinstein, M., Durand, F., Freeman, W.T.: Riesz pyramids for fast phase-based video magnification. In: *2014 IEEE International Conference on Computational Photography (ICCP)*. pp. 1–10. IEEE (2014)
16. Wu, H.Y., Rubinstein, M., Shih, E., Guttag, J., Durand, F., Freeman, W.: Eulerian video magnification for revealing subtle changes in the world. *ACM transactions on graphics (TOG)* **31**(4), 1–8 (2012)
17. Zhang, Y., Pinteá, S.L., Van Gemert, J.C.: Video acceleration magnification. In: *Proceedings of the IEEE Conference on Computer Vision and Pattern Recognition*. pp. 529–537 (2017)
18. Zhao, K., Han, Q., Zhang, C.B., Xu, J., Cheng, M.M.: Deep hough transform for semantic line detection. *IEEE Transactions on Pattern Analysis and Machine Intelligence* **44**(9), 4793–4806 (2021)
19. Zhou, X., Koltun, V., Krähenbühl, P.: Tracking objects as points. In: *European conference on computer vision*. pp. 474–490. Springer (2020)